Nano Energy 67 (2020) 104252

Contents lists available at ScienceDirect

Nano Energy

journal homepage: http://www.elsevier.com/locate/nanoen

Full paper

Unraveling (electro)-chemical stability and interfacial reactions of $Li_{10}SnP_2S_{12}$ in all-solid-state Li batteries

Bizhu Zheng [a], Xiangsi Liu [a], Jianping Zhu [a], Jun Zhao [e], Guiming Zhong [c], Yuxuan Xiang [a], Hongchun Wang [b], Weimin Zhao [b], Ediga Umeshbabu [a], Qi-Hui Wu [d], Jianyu Huang [e], Yong Yang [a,b,*]

[a] Collaborative Innovation Center of Chemistry for Energy Materials, State Key Laboratory for Physical Chemistry of Solid Surface, College of Chemistry and Chemical Engineering, Xiamen University, Xiamen, 361005, China
[b] College of Energy, Xiamen University, Xiamen, 361005, China
[c] Xiamen Institute of Rare Earth Materials, Haixi Institutes, Chinese Academy of Sciences, Xiamen, 361024, China
[d] College of Mechanical and Energy Engineering, Jimei University, Xiamen, 361021, China
[e] Clean Nano Energy Center, State Key Laboratory of Metastable Materials Science and Technology, Yanshan University, Qinhuangdao, 066004, China

ARTICLE INFO

Keywords:
$Li_{10}SnP_2S_{12}$
Stability
Solid state NMR
All solid-state batteries
Interfacial kinetic

ABSTRACT

$Li_{10}SnP_2S_{12}$ (LSPS) with high ionic conductivity and moderate price is a promising solid electrolyte for all-solid-state batteries. However, the instability of LSPS and LSPS/electrodes interfaces would cause poor cycle performance issues in the LSPS-based all-solid-state batteries, which have not been well understood. Herein, we address and unravel the decomposition products of LSPS and their Li^+ transfer characteristics, especially on the surface of LSPS/electrodes by using solid-state nuclear magnetic resonance (ss NMR) spectroscopy coupled with X-ray photoelectron spectroscopy (XPS). The results reveal that the high mechanical energy during ball-milling process leads to the decomposition of LSPS into Li_4SnS_4 and Li_3PS_4. During charge/discharge cycling, specific capacity fading of batteries originates from the formation of new interfacial layer at LSPS/Acetylene black cathode and LSPS/Li metal anode interfaces. Furthermore, our results demonstrate that the rough and porous morphology of the interface formed after cycling, rather than the decomposition products, is the critical factor which results in the increases of the interfacial resistance at LSPS/Li interface and serious formation of Li dendrite. Our results highlight the significant roles of (electro)chemical and interfacial stability of sulfide solid electrolyte in the development of all-solid-state batteries.

1. Introduction

Lithium ion batteries have achieved great success as one of the most widely acceptable power sources for portable electronic devices and electric vehicles. As energy demands increase due to the exponential development of new technologies, more efficient Li-ion batteries with higher energy density, longer cycle life and higher safety are required. Nevertheless, in the case of liquid electrolyte-based lithium ion batteries, many of the issues including the limit of energy density and the concern of safety are still urgent to be solved. The removal of organic solvents can effectively reduce the flammability of lithium batteries. Hence, all-solid-state lithium batteries have received a lot of attention owing to their high energy density and excellent safety, where a solid state electrolyte serves as both battery separator and ionic conductor [1]. Solid state electrolytes (SSEs) are considered to inherently improve the safety and enhance the energy density of lithium batteries for their non-flammability, less stringent packaging demands and good mechanical strength enabling the use of Li metal in all-solid-state batteries. In addition, all-solid-state batteries can further widen the working temperature range, facilitating the use of batteries in some extreme circumstances. The key issues for all-solid-state batteries are how to design and develop suitable SSEs and fabricate compatible and stable interfaces between electrodes and SSEs. Sulfide SSEs possess a lot of advantages including high room-temperature ionic conductivity, low grain boundary resistance and their good contact with electrode materials due to their mechanical softness compared to oxides. Despite

* Corresponding author. State Key Laboratory for Physical Chemistry of Solid Surface, College of Chemistry and Chemical Engineering, Xiamen University, Xiamen, 361005, China.
E-mail addresses: yyang@xmu.edu.cn, 1661049287@qq.com (Y. Yang).

https://doi.org/10.1016/j.nanoen.2019.104252
Received 9 July 2019; Received in revised form 30 October 2019; Accepted 31 October 2019
Available online 4 November 2019

tremendous progress have been made in developing SSEs with high ionic conductivities [2,3], the rate capability of all-solid-state batteries is still unsatisfactory for the incompatibility at electrode/SSEs interface, mainly due to the narrow electrochemical window of SSEs which leads to side reaction at electrode/SE interface and poor solid/solid contact during cycling [4]. The properties of SSEs and the compatibility of electrode/SSEs interface govern the rate capability, cycle life and safety of all-solid-state batteries. Therefore, it is critical to get a comprehensive understanding of the properties of SSEs, including ionic conductivities, chemical and electrochemical stability and point out the superiority and key issues of SSEs employed in all-solid-state batteries, and then to design possible solutions to optimize the SSEs by element doping or to modify the electrode/SSEs interface.

$Li_{10}GeP_2S_{12}$ (LGPS) with an extremely high ionic conductivity (12 mS cm^{-1}, RT) was firstly reported by Kanno's group [3]. So far, many works have already offered insights in the electrochemical stability and the decomposition products of LGPS based on theoretical calculations [5,6] and experimental demonstration [7–9]. For example, Han et al. assembled a single all-solid-sate battery based on LGPS as solid electrolyte, cathode and anode materials, indicating that LGPS is redox active in all-solid-state batteries [7]. Furthermore, Wenzel et al. studied the chemical reaction at Li/LGPS interface via in-situ X-ray photoelectron spectroscopy (XPS), revealing that the decomposition of LGPS leads to the formation of an interphase composed of Li_3P, Li_2S, and Li−Ge alloy at LGPS/Li interface [9]. In addition, Kanno's group analyzed the chemical reaction at cathode/LGPS interface in the high voltage all-solid-state batteries consisting of $LiNi_{0.5}Mn_{1.5}O_4$ cathode, LGPS solid-electrolyte, and Li metal anode [8]. They pointed out that it is essential to choose a suitable conductive additive in cathode composite. In 2013, Bernhard Roling's group synthesized the analogue of LGPS—$Li_{10}SnP_2S_{12}$ (LSPS) [10]. When compared with expensive Ge element, the precursors of LSPS are much cheaper. Moreover, the less expensive tin-based analogue LSPS has very high values of 7 mS cm^{-1} for the grain conductivity and 4 mS cm^{-1} for the total conductivity at room temperature. The low cost and high ionic conductivity give this material a large advantage for application in all-solid-state batteries. Although, in 2012, Ceder group [11] have already presented a detailed theoretical investigation of the phase stability, electrochemical stability and Li^+ conductivity of the $Li_{10\pm1}MP_2X_{12}$ (M=Ge, Si, Sn, Al or P, and X=O, S or Se) family. However, there is not much experimental information available on LSPS material, especially on the structural stability and electrochemical properties of LSPS.

Apparently, formation of favorable solid–solid contacts between electrode and electrolyte is important in all-solid-state batteries. When preparing the cathode composite in both solid and liquid electrolyte batteries, planetary ball-milling processing method is an effective technique to ensure uniform and thorough stirring in which the artificial gravity generated by the centrifugal force can be applied to the grinding medium. Besides, it is worth noting that the high mechanical energy, released at the point of collision between balls as well as the friction of balls on the wall, could transfer to the bulk materials and affect their phase stability. Considering the poor phase stability of sulfide SSEs, the feasibility of utilization of ball-milling processing method in all-solid-state batteries still lack for further study. In addition, for facilitating the best use of LSPS sulfide solid electrolyte in the practical application of all-solid-state batteries, it is essential to get a thorough understanding of the intrinsic (electro)chemical stability of this material and address the high interfacial resistance issues in LSPS based all-solid-state batteries.

In this work, in order to analyze the effect of mechanical energy on the phase stability of LSPS material during processing, a detailed comparative study has been made on LSPS sulfide SSE under grinding or ball-milling. In addition, XPS, ss NMR measurements coupled with several techniques have been conducted to shed light on the interfacial reaction at both LSPS/Acetylene black (AB) cathode and LSPS/Li anode interfaces in all-solid-state batteries, where $Li_4Ti_5O_{12}$@$LiCoO_2$ acts as cathode, LSPS acts SSEs and Li metal acts as anode. This study would give a unique insight in the transfer kinetics over the LSPS/Li interface, which appears vital for the power performance of all-solid-state batteries.

2. Material and methods

2.1. Preparation of batteries

2.1.1. The fabrication of LTO@LCO/LSPS/Li all-solid-state batteries

$Li_4Ti_5O_{12}$@$LiCoO_2$ (LTO@LCO) (Xiamen Tungsten Co., Ltd) as cathode active material is mixed with LSPS solid electrolyte (NEI Corporation) and Acetylene black (AB) with a weight ratio of 50:48:2 by using a mortar for 30 min to obtain cathode composite. 130 mg LSPS powder is cold pressed into pellet, 10 mm in diameter, with the pressure of 510 MPa. And 4 mg cathode composite is pressed on the surface of LSPS pellet with the same pressure. A piece of Li metal is subsequently attached to the other side of LSPS pellet and pressed by hand. Finally, the LTO@LCO/LSPS/Li all-solid-state batteries are put in the custom-made molds. (LSPS + AB)/LSPS/Li all-solid-state batteries are assembled with the same method, where cathode composite is prepared by mixing LSPS and AB with the weight ratio of 50:3.

2.1.2. The fabrication of liquid-electrolyte batteries

Liquid electrolyte batteries based on LTO@LCO cathode active material are assembled as coin-type cells. The cathode electrodes are fabricated by casting a slurry consisting of 80 wt% LTO@LCO active material, 10 wt% AB as the conductive additive, and 10 wt% polyvinylidendifluoride (PVdF) solved in N-methylpyrrolidone (NMP) as a binder on an aluminum foil. Lithium metal is used as a counter electrode. The electrolyte solution is 0.1 mol/L LiTFSI and 1 mol/L $LiBF_4$ in ethylene carbonate (EC) and dimethyl carbonate (DMC) mixture (1:1 ratio by weight).

2.1.3. The fabrication of Li/LSPS/Li and C/LSPS/C symmetric cells

130 mg LSPS powder is pressed into pellet with the pressure of 510 MPa. Li/LSPS/Li symmetric cell is assembled by attaching Li metal to both sides of LSPS pellet and pressing them by hand. C/LSPS/C symmetric cell is assembled by attaching carbon foil to both sides of LSPS pellet and pressing them with the pressure of 510 MPa.

2.2. Electrochemical measurements

Galvanostatic charge and discharge measurements of the batteries were conducted on a LAND CT-2001A (Wuhan, China) battery test system at room temperature (RT). The electrochemical impedance spectroscopy (EIS) measurements were carried out by using a Versa STAT MV Multichannel potentiostat/galvanostat (Princeton Applied Research) from 1 Hz to 1 MHz with an amplitude of 10 mV at RT. CV measurements are conducted by using a Versa STAT MV Multichannel potentiostat/galvanostat (Princeton Applied Research).

2.3. Characterization of materials

X-ray powder diffraction (XRD) analyses were performed by a Rigaku Ultima IV powder X-ray diffractometer using a Cu Kα radiation ($\lambda = 1.5406$ Å), and Mylar film was used to seal the sample to avoid reactions between the solid electrolyte and moist air. Scanning electron microscopy (SEM, Hitachi S-4800) and energy dispersive spectrometer (EDS) were utilized to characterize the morphology and element distribution of the materials. A scanning electron microscope/focused ion beam (FIB/SEM) device (FEI-Helios-G4) was perpendicular to the sample which allows cross-sectional micro milling to get the cross-section images of LTO@LCO. X-ray photoelectron spectroscopy (XPS) was carried out on a PHI 5000 Versa Probe III spectrometer (ULVAC-PHI, Japan) on the sample surface using argon ion beam gun operating at

25.1 W. The binding energy scale was calibrated from the hydrocarbon contamination using the C 1s peak at 284.8 eV. For SEM and XPS characterizations, an airtight specimen holder is used to avoid moisture and air contamination during sample transfer.

Ex-situ ^{6}Li, ^{31}P and ^{119}Sn magic-angle spinning (MAS) nuclear magnetic resonance (NMR) spectroscopy were acquired on a Bruker AVANCE III 400 MHz spectrometer, all experiments were carried out using a double resonance 1.3 mm MAS probe, spinning at frequencies of up to 50 kHz with a single pulse sequence (90° pulse, 90° pulse and 30° pulse for ^{6}Li, ^{119}Sn and ^{31}P, respectively). For ^{6}Li MAS NMR, the 90° pulse length was 1.10 μs and the recycle delay was 1.5 s. The ^{6}Li shifts were referenced to LiF (-1 ppm), at a ^{6}Li Larmor frequency of 58.89 MHz. For ^{31}P MAS NMR, the 30° pulse length was 0.53 μs and the recycle delay was 160 s. The ^{31}P shifts were referenced to ADP (1 ppm), at a ^{31}P Larmor frequency of 162.02 MHz. The 90° pulse length for ^{119}Sn was 1.20 μs and the recycle delay was 20 s. All the ^{119}Sn shifts were referenced to SnO_2 (-604 ppm). T_1 relaxation times for the ^{6}Li MAS NMR were determined using a saturation recovery experiment at 50 kHz.

3. Results and discussion

3.1. The electrochemical performance of all-solid-state batteries and liquid electrolyte batteries

In this study, the LSPS solid state electrolyte powder was purchased from NEI Corporation. And the material we use shows the ionic conductivity of 2.7 mS cm^{-1} (Fig. S3) and fits very well with the XRD pattern card (Fig. S2). Electrochemical performance of all-solid-state battery (**SSB**) (Fig. 1(a)) and liquid electrolyte battery (**LIB**) (Fig. 1 **(b)**) was studied and compared by performing galvanostatic cycling experiments under constant current density of 0.1 C (1 C=120 mA g^{-1}) and the voltage range of 2.8–4.2 V at room temperature. Fig. 1(c) presents the initial charge-discharge curves of both batteries. The initial charge and discharge capacity of liquid electrolyte battery are 149 mAh g^{-1} and 138 mAh g^{-1}, respectively, resulting in a high coulombic efficiency of 93%. In stark contrast, the LTO@LCO/LSPS/Li all-solid-state battery delivers initial charge capacity of 172 mAh g^{-1} and discharge capacity of 132 mAh g^{-1} with a significantly lower coulombic efficiency of 77%. After 70 cycles, the reversible capacity decays to 84 mAh g^{-1} or 64% of initial discharge capacity (Fig. 1(e) and Fig. S4). As observed in Fig. 1(c) and **(d)**, during the charging periods, LIB shows a single charge plateau at 3.9 V while SSB shows an additional slope at 2.8 V, which may originate from the decomposition of LSPS electrolyte. The apparent difference between SSB and LIB electrochemical performance has a great relationship with the properties of LSPS solid electrolyte, so a more thorough and detailed investigation of LSPS material is required.

Actually, plenty of work have offered insight in the redox reaction of LGPS material at cathode and anode side [7–9]. But there is not much experimental research on the chemical and electrochemical reaction of LSPS in all-solid-state batteries. Thus, in order to clarify the strange phenomena in the electrochemical performance of LTO@LCO/LSPS/Li all-solid-state batteries, we focus on the chemical and electrochemical behavior of LSPS at both cathode and anode sides and the interfacial kinetic of all-solid-state batteries in the following research. Because a uniform coating layer $Li_4Ti_5O_{12}$ is successfully introduced into LCO/LSPS interface as indicated by the FIB and EDS mapping results in Fig. S1. There may still exist little side reaction between LCO/LSPS interface, but it is not the main issue we need to concern in this work. For the cathode side, here we mainly consider the side reaction between LSPS/AB.

3.2. The structural stability of LSPS

When preparing cathode composite, high energy ball-milling is an

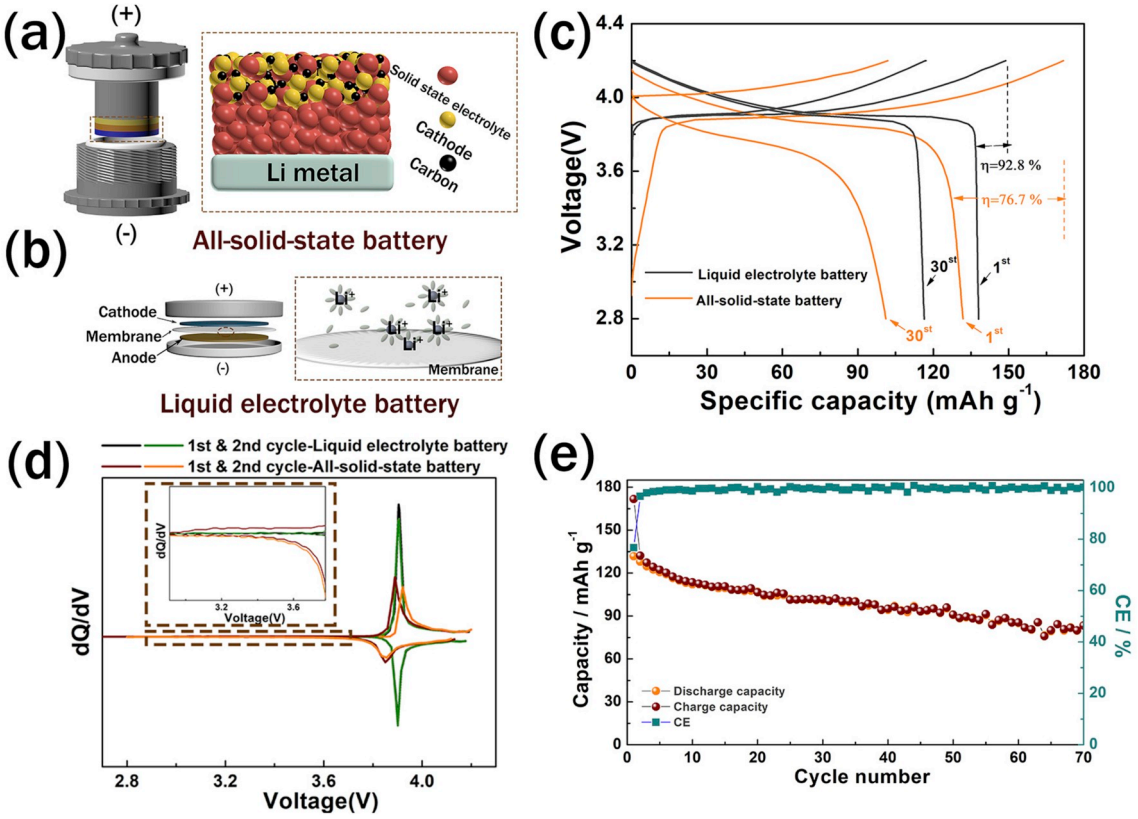

Fig. 1. The electrochemical performances of $Li_4Ti_5O_{12}$@$LiCoO_2$/LSPS/Li all-solid-state batteries and $Li_4Ti_5O_{12}$@$LiCoO_2$/Li liquid electrolyte batteries. The schematics of (a) all-solid-state battery and (b) liquid electrolyte battery. (c) The initial charge and discharge curves, (d) dQ/dV curves of all-solid-state battery and liquid electrolyte battery and (e) cycle performance of all-solid-state battery at room temperature.

effective and extensively used processing method in liquid electrolyte batteries and even in some all-solid-state batteries due to the fact that it provides a uniform and thorough mixture of cathode material [12–15]. However, what cannot be ignored is the high mechanical energy produced from the collision between different sizes of balls as well as the friction of balls to wall during ball-milling. Therefore, considering the poor phase stability of sulfide SSEs, it is vital to analyze the impact of mechanical energy on the structural stability of LSPS during preparing composite process for all-solid-state batteries. Herein, we report a comparative study on pristine LSPS powder and LSPS powder treated with hand-grinding for 30 min using a mortar or high energy planetary ball-milling at 350 or 500 rpm for 30 min in Ar atmosphere. Then, to gain a better understanding of the chemical stability of LSPS solid electrolyte, X-ray diffraction (XRD), Scanning electron microscope (SEM), Electrochemical Impedance Spectroscopy (EIS) and Solid State Nuclear Magnetic Resonance (ss-NMR) techniques are conducted to analyze the difference of LSPS powder with different treatments.

The XRD pattern (Fig. 2(a)) indicates that no obvious change occurs between the structures of LSPS powder before and after grinding. Nevertheless, the crystallinity of LSPS decreases with the increase of the ball-milling rotation rate. Especially, at the condition of 500 rpm ball-milling, the corresponding diffraction peaks in the XRD pattern disappear and the peak at 26.3° is related to Mylar membrane, indicating the almost complete amorphization of LSPS material during the 500 rpm ball-milling process. Fig. 2**(c–j)** compare the SEM images of LSPS powder with different treatments. Apparently, the size of pristine LSPS powder exhibits uneven distribution. The large particle is approximately 20–50 μm (Fig. 2(c, g)), and the size decreases to 10–20 μm after hand-grinding (Fig. 2(d, h)). Whereas for the LSPS powder after ball-milling, the grain sizes decrease into 5–10 μm at 350 rpm ball-milling (Fig. 2(e, i)) and 2–4 μm at 500 rpm ball-milling (Fig. 2(f, j)). To further verify the effect of different treatment on the ionic conductivity, EIS spectra and the summary of fitting results are presented in Fig. 2(b) and Table. S1. It is obvious that both grain and total ionic conductivities decrease in this order: $\sigma_{pristine} > \sigma_{grinding} > \sigma_{350\ rpm\text{-}ball\text{-}milling} > \sigma_{500\ rpm\text{-}ball\text{-}milling}$. The decrease in ionic conductivity of LSPS after grinding and ball-milling may correspond to the existence of impurities and the reducing particle size which leads to high grain boundary resistance. Furthermore, a comparative study on the electrochemical performance of all-solid-state batteries based on ball-milled with 350 rpm and 500 rpm or hand-grind LSPS material has been shown in Fig. 3. Consistent with the EIS results, the batteries with 350 or 500 rpm ball-milled LSPS deliver the decreasing discharge capacity with the value of 111 and 107 mAh g^{-1}, respectively. But they didn't show apparent difference in the capacity retention and initial CE. It is further proved that ball-milling procedure is detrimental to the electrochemical performance of LSPS based all solid-state batteries, and the capacity of all solid-state batteries decreases with the increase of the rotation rate of ball-milling procedure.

In addition, the chemical composition of the LSPS with different treatments was analyzed by ss NMR, which is sensitive to local environment and widely used for substance identification. As shown in Fig. 4 (b), the ^{31}P NMR spectrum of pristine LSPS material exhibits two main peaks at 92.3 ppm and 76.7 ppm, associated with the P(1) and P(2) sites in $Li_{10}SnP_2S_{12}$, respectively [16]. Other three weak peaks are observed at 86.9, 83.6 and 71.8 ppm, due to the signals of Li_7PS_6 [16,17], Li_3PS_4 [18] and Li_2PS_3 [17], respectively. The ^{119}Sn NMR spectrum (Fig. 4(c)) gives rise to a strong peak at 86.0 ppm ascribed to Sn on the 4d site of $Li_{10}SnP_2S_{12}$ and a weaker peak at 77 ppm, possibly corresponding to

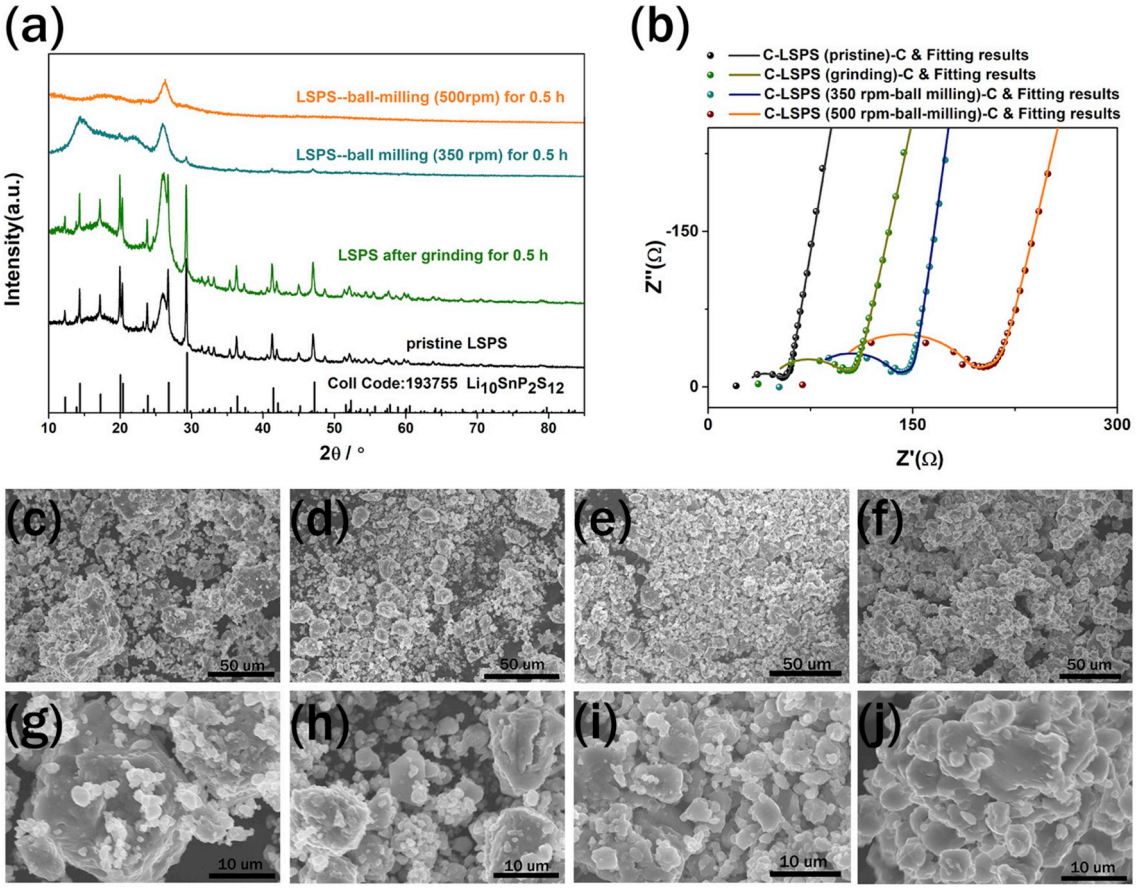

Fig. 2. The structure, morphology and electrochemical impedance of LSPS with different treatments. (a) XRD pattern, (b) EIS of C/LSPS/C symmetric cells. SEM imagines of (c) and (g) pristine LSPS powder, (d) and (h) LSPS powder after hand-grinding, (e) and (i) LSPS powder after 350 rpm ball-milling, (f) and (j) LSPS powder after 500 rpm ball-milling.

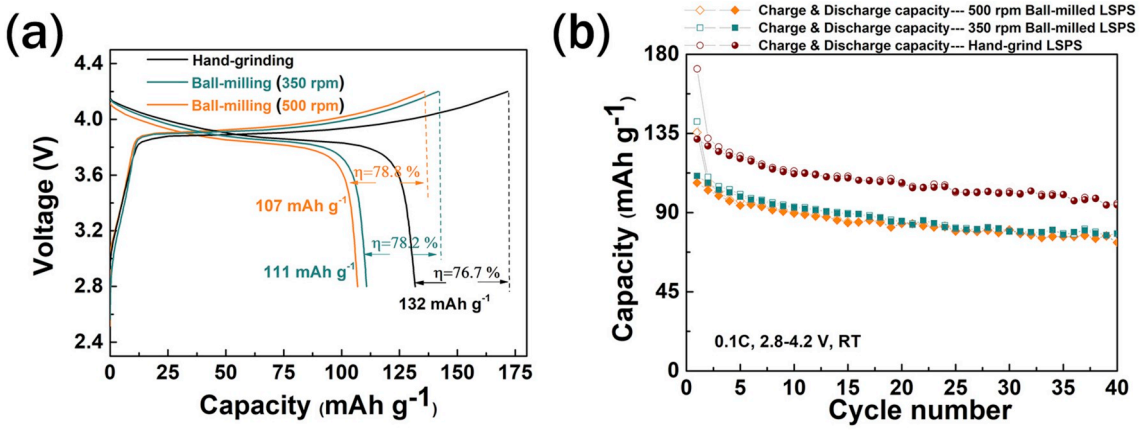

Fig. 3. (a) The initial charge and discharge curves and (b) cycle performance of LTO@LCO/LSPS/Li all-solid-state batteries based on hand-grind or ball-milled LSPS material.

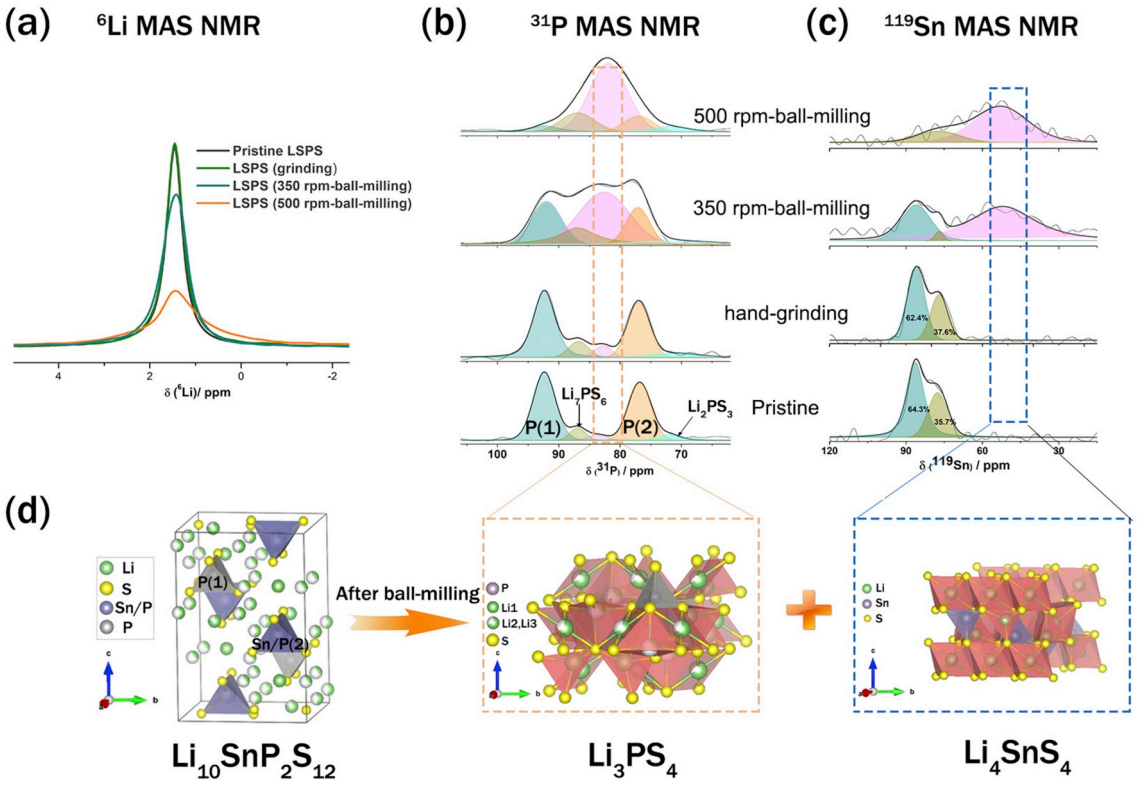

Fig. 4. The ss-NMR results of LSPS material before and after treatments. (a) ^{6}Li, (b) ^{31}P, and (c) ^{119}Sn MAS NMR spectra of the LSPS powder with different treatment. (d) The decomposition mechanism of LSPS powder after ball-milling.

some cation disorder in the main phase as described in literature [16]. Due to the fast exchange rate, the different Li sites could not be distinguished even for high resolution ^{6}Li spectra (Fig. 4(a)), but it is helpful to confirm whether some side reactions have occurred or not. After grinding, the impurities in the ^{31}P and ^{119}Sn NMR spectra show minimal enhancement and ^{6}Li spectrum is almost the same as the pristine sample. By comparison, the ^{31}P NMR spectrum of LSPS powder after ball-milling is dominated by Li_3PS_4. And a broad peak at 52 ppm is observed in the ^{119}Sn NMR spectrum, revealing the presence of Li_4SnS_4[19]. Besides, the half width of the signal becomes wider significantly after ball-milling in the ^{6}Li NMR spectrum, indicating that some Li sites corresponding to side reaction product generate and the Li^+ mobility become slower. The results in ^{6}Li, ^{31}P and ^{119}Sn ss NMR spectra reveal that the amount of impurity significantly enhances with the increase of ball-milling rotation rate. Thus, our ss NMR data indeed confirm that LSPS decomposes after ball-milling according to the reaction (Fig. 4(d)): $Li_{10}SnP_2S_{12}$=2Li_3PS_4+Li_4SnS_4. As reported in the literature, the ionic conductivities of Li_4SnS_4 and Li_3PS_4 are 7×10^{-5} S cm^{-1} (RT) [19] and 2×10^{-4} S cm^{-1} (RT) [18,20], respectively, both of which are lower than that of LSPS. Such observations account for the decrease in the ionic conductivity and greatly support the results in Fig. 2(b).

It thus can be concluded from the results above that LSPS is prone to decomposing during ball-milling and even grinding can lead to the generation of minimal impurities in LSPS material, which are detrimental to the ionic conductivity. The decomposition of LSPS after ball-milling is because during the process of milling, ceramic powders are deformed and fractured many times, and the mechanical energy released from the friction of balls transfers to LSPS material and affect its

phase. The results are consistent with the theoretical results [11] where the decomposition energy of LSPS is 25 meV per atom, and the equilibrium phases comprise Li_4SnS_4 and Li_3PS_4. The mechanical energy generated from hand-grinding is quite low, which is not enough to cause the decomposition of LSPS. Under the condition of ball-milling, when compared to the rotation rate of 350 rpm, ball-milling at 500 rpm provides much higher mechanical energy than the decomposition energy, thus accelerating the complete decomposition of all LSPS material. It thus is crucial to consider how to ensure homogenous mixing without compromising the electrochemical performance of sulfide solid electrolyte based all solid-state batteries when preparing the cathode composite. Herein, hand grinding is more suitable to prepare the cathode composite based on LSPS solid electrolyte. And all composites in the following research are prepared by grinding with a mortar.

3.3. The electrochemical stability at electrode/LSPS interface

3.3.1. The electrochemical stability at LSPS/Acetylene black (AB) interface

In order to clarify the side reaction and the electrochemical behavior of LSPS at the LSPS and AB composite, CV measurements are conducted on the (LSPS + AB)/LSPS/Li all-solid-state batteries, where (LSPS + AB) composite acts as work electrode and Li metal acts as counter electrode. For the positive scan (Fig. S5(a)), a prominent oxidation peak is observed at approximately 2.8 V and for the negative scan (Fig. S5(b)), a reduction peak is observed at approximately 1.4 V. Furthermore, when positively scanning at the voltage range of 2.8–4.3 V (Fig. S5(c)), it only exhibits an irreversible oxidation peak, the current intensity of which decreases with the cycles. In great agreement with the CV results, the (LSPS + AB)/LSPS/Li all-solid-state cell only shows an initial charge capacity of 24 mAh g^{-1} during cycling (Fig. S5(d)), hinting at the oxidative decomposition of LSPS. The experimental results reveal that the solid electrolyte is redox active and (LSPS + AB) composite is only stable at 1.4–2.8 V.

XPS analysis was performed on pristine LSPS pellet, the pristine (LSPS + AB) composite material and (LSPS + AB) composite after charged to 4.2 V to ascertain the side reaction at the (LSPS + AB) composite (Fig. 5). It is obvious that pristine LSPS and pristine (LSPS + AB) composite show no significant difference in S 2p, P 2p and Sn 3d XPS spectra. And for these three samples, in S 2p XPS spectra, a broad sulfur peak emerges as a doublet at 162.6 eV and 161.3 eV due to S^{2-} in LSPS structure. However, for the (LSPS + AB) composite after charged to 4.2 V, higher energy doublets at 163.6 eV and 164.6 eV are attributed to the formation of S_8^{21}. Moreover, in P 2p XPS spectra of composite material after charged to 4.2 V, the higher energy doublets at 133.60 eV and 132.7 eV can be assigned into the oxidized phosphorus species [21]. And both peaks in Sn 3d XPS spectra of composite material after charged to 4.2 V shift to higher energies of 492.3 eV and 486.9 eV, due to the formation of SnS_2 [22]. Therefore, it can be concluded from the XPS results that, oxidation reaction of LSPS solid electrolyte exists at the (LSPS + AB) composite when charged to 4.2 V, confirmed by the presence of S_8, oxidized phosphorus species and SnS_2. Herein, the oxidation reaction for LSPS solid electrolyte is given as: $Li_{10}SnP_2S_{12}=10Li^+ + 5S + SnS_2 + P_2S_5 + 10e^-$.

Consequently, the irreversible slope at 2.8 V in the charge curve of LTO@LCO/LSPS/Li (Fig. 1(c)) is related to the oxidation of LSPS material and is considered to have a significant contribution to the large initial irreversible capacity and low initial coulombic efficiency of LTO@LCO/LSPS/Li all-solid-state batteries. Our results demonstrate that most of the interface layer formation at LSPS/AB takes place in the first cycle when charging to potentials above 4.2 V vs Li^+/Li. Furthermore, the high resistance nature of S_8 in the products may increase the polarization of cells.

3.3.2. Electrochemical stability at the LSPS/Li metal interface

Fig. 6(a) and **(d)** show the voltage profiles of Li/LSPS/Li symmetric cell and the EIS spectra of symmetric cell before and after cycling for 66 h. As the cycle number increases, the resistance of cell increases dramatically (Fig. 6(d)), as indicated by the increasing overpotential of symmetric cell during Li plating and stripping (Fig. 6(a)). Fig. 6(b) and **(c)** are corresponding optical camera images of Li metal and LSPS pellet after cycling, in which both Li metal and LSPS pellet turn black after cycling, suggesting that the side reaction occurs at the Li/LSPS interface.

The morphology of the pristine (Fig. 7(a, b)) and cycled LSPS pellet (Fig. 7**(c–f)**) was examined by SEM. The results confirm that pristine LSPS pellet shows relatively dense and flat surface. On the contrary, the cycled LSPS pellet shows loose and porous surface induced by the volume expansion after interfacial reaction, resulting in a poor contact between LSPS/Li metal. And even something like Li dendrite (Fig. 7(f)) appears at the crack of LSPS pellet, causing the capacity degradation of Li/LSPS/Li cell.

To further identify the chemical composition of LSPS/Li interface after cycling, the XPS measurements are conducted on the surface of cycled Li metal excluding the influence of LSPS bulk pellet. And ss NMR measurements are performed on the cycled LSPS powder scraped from the cycled LSPS/Li interface. As shown in Fig. 8(a), XPS results confirm that after cycling with Li metal, LSPS is reduced into Li_2S, Li_3P and Li-Sn alloy, in good overall agreement with the results from Ceder group's calculation results [11]. That is, the reduction of LSPS can be described as: $Li_{10}SnP_2S_{12}+21e^-+21Li^+=12Li_2S+2Li_3P$ + Li-Sn. In ss NMR results (Fig. 8(c)), it is interesting to observe that, a ^{31}P NMR peak appears at

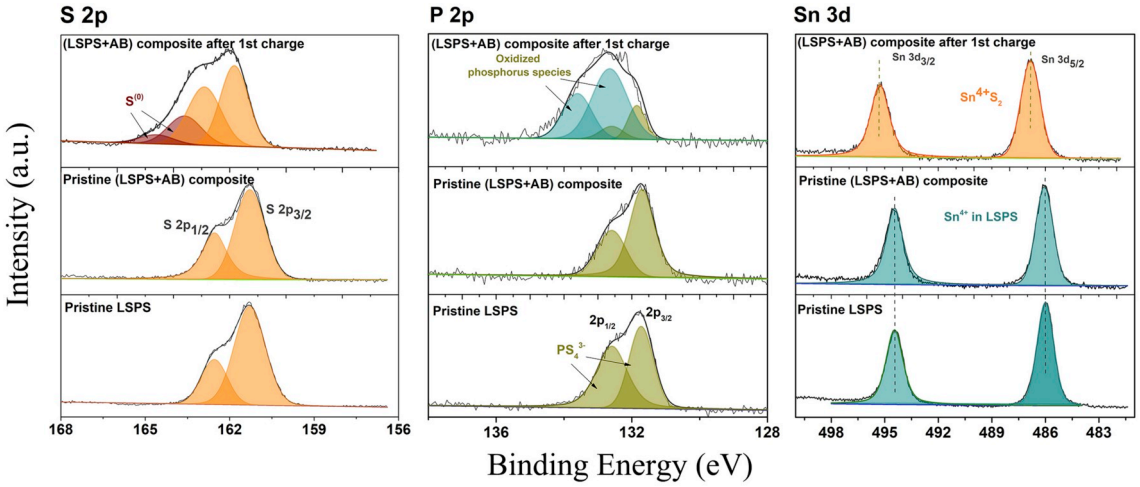

Fig. 5. X-ray photoelectron spectra of the pristine LSPS, (LSPS + AB) composite before and after charged to 4.2 V.

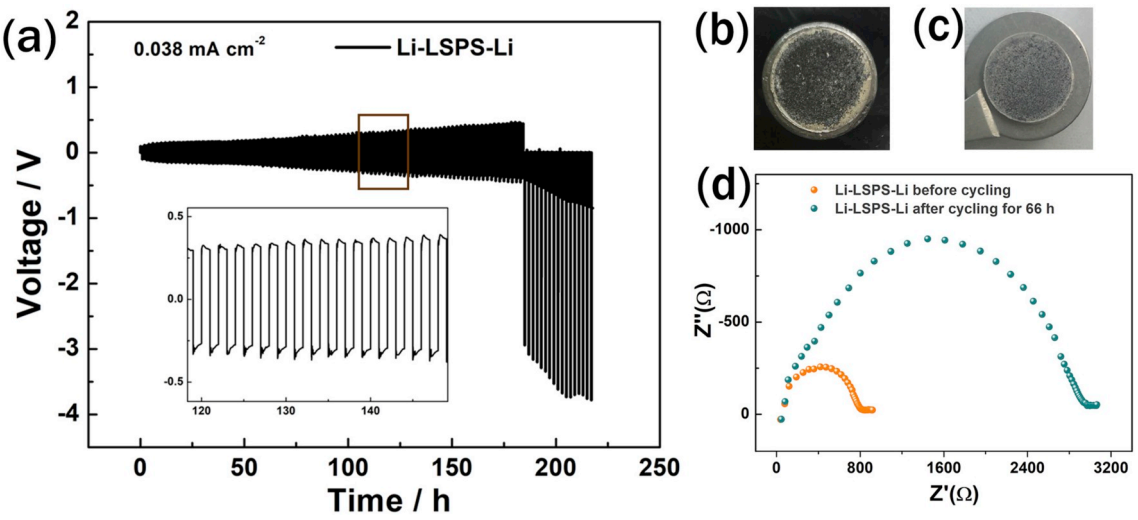

Fig. 6. The electrochemical performance of Li/LSPS/Li symmetric cell. (a) The Li^+ plating and stripping curves of Li/LSPS/Li symmetric cell, the optical camera images of (b) the cycled Li metal and (c) the cycled LSPS pellet, and (d) EIS spectra of Li/LSPS/Li before and after cycling for 66 h.

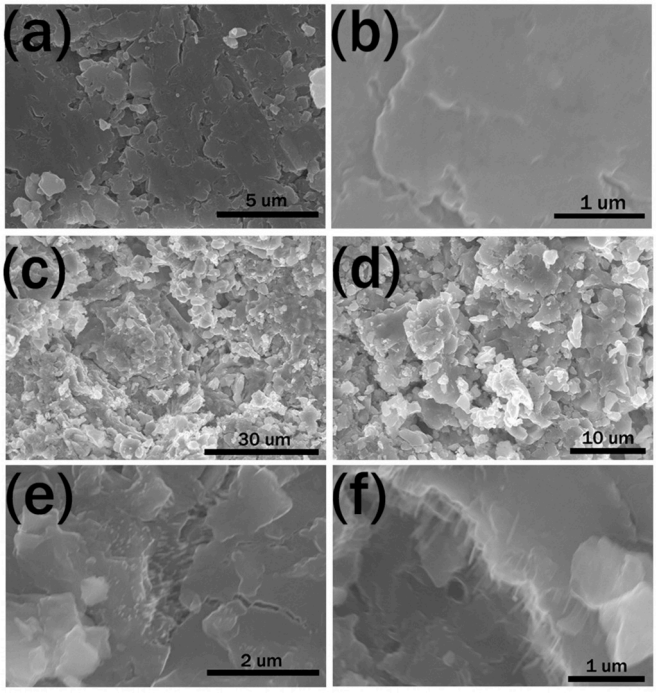

Fig. 7. The morphology of pristine and cycled LSPS pellets. SEM images of (a, b) the surface of pristine LSPS pellet, (c–f) the surface of the cycled LSPS pellet.

-310 ppm which we consider as an off-stoichiometry phase of "$Li_{3+x}P$" for the excess lithiation of Li_3P, also reported in our previous work [23]. And the broad ^6Li NMR peak at 3.9 ppm is assigned to Li_3P and $Li_{3+x}P$. Generally, a shorter T_1 indicates a higher Li^+ mobility for Li^+ SSEs. Herein, ^6Li T_1 is used to compare the Li ion transfer kinetics over pristine LSPS and the decomposition phase of LSPS/Li interface after cycling. The Spin-lattice relaxation times T_1 are given for pristine LSPS and cycled LSPS in Fig. S6 and Table S2. The black curve corresponding to the pristine LSPS exhibits T1 value of 857 ms, and orange curve with T1 value of 899 ms is related to the bulk LSPS material at the LSPS/Li interface. Furthermore, the green curve can be fitted with two components, consistent with the two peaks of Li_3P and Li_2S in Fig. 8(b). The results show that T_1 values of Li_3P and Li_2S are 193 ms and 872 ms, respectively, which are similar or even much smaller than that of pristine LSPS material. It suggests the enhanced Li ion transport properties for the new compounds produced during cycling. However, it is noteworthy that Li_3P shows ionic conductivity 10^{-4} S cm^{-1} and the ionic conductivities of bulk and nano Li_2S are 10^{-13} and 10^{-11} S cm^{-1} at room temperature, respectively, several orders of magnitude lower than that of LSPS in literature [24,25]. As has been demonstrated for other nanostructured material by A. Dunst et al. [26], mechanical treatment can largely increase the overall conductivity of Li_2O_2 by more than two orders of magnitude for the defects generated in both the bulk and the surface-influenced regions of Li_2O_2. Moreover, Yelong Zhang and co-workers [27] confirm that the morphology of Li_2O_2 impacts strongly on the ionic conductivity. That is, amorphous Li_2O_2, compared with its crystalline siblings, possess improved ionic transport properties suggested by the smaller T_1. Therefore, we infer that the higher Li mobility of Li_3P and Li_2S at LSPS/Li interface is most likely related to other factors, including the structural properties (amorphous or nanocrystalline) and the defect chemistry of Li_3P and Li_2S. Therefore, the main factor resulting in an increased interfacial resistance at LSPS/Li interface is attributed to the porous and loose surface morphology of the cycled LSPS pellet which may be resulted by the volume expansion after reduction reaction. In other words, the deterioration of formerly compact solid/solid contact during cycles leads to the lose interfacial contact and reduction of Li ion conducting channel, thus severely hindering the transport of lithium ions at the LSPS/Li interface. It has been further confirmed by the EIS results in Fig. S7 that hand-pressing the Li electrode after cycling again can greatly improve the solid/solid contact, as indicated by the decreased interfacial resistance of the cycled Li/LSPS/Li symmetric cell. Moreover, the mixing electronic and ionic conducting layer promotes the formation of Li dendrite at the Li/LSPS interface, accounting for the results in Fig. 7f. Consequently, it is imperative to modify the interface between Li/LSPS to further improve the stability of LSPS against Li metal. Several strategies have been utilized to stabilize the interface at Li/sulfide solid electrolyte, including using alloy as anode, double-layer SSE configuration or interposing a buffer layer at the interface. In our previous work [28], a small amount of ionic liquid is utilized to modify the surface of LSPS pellet for the in-situ formed solid electrolyte interface (SEI) layer.

4. Conclusion

In this paper, we demonstrate that LSPS suffers severe chemical decomposition during ball-milling processing which provides extremely high mechanical energy to the bulk LSPS material, leading to the

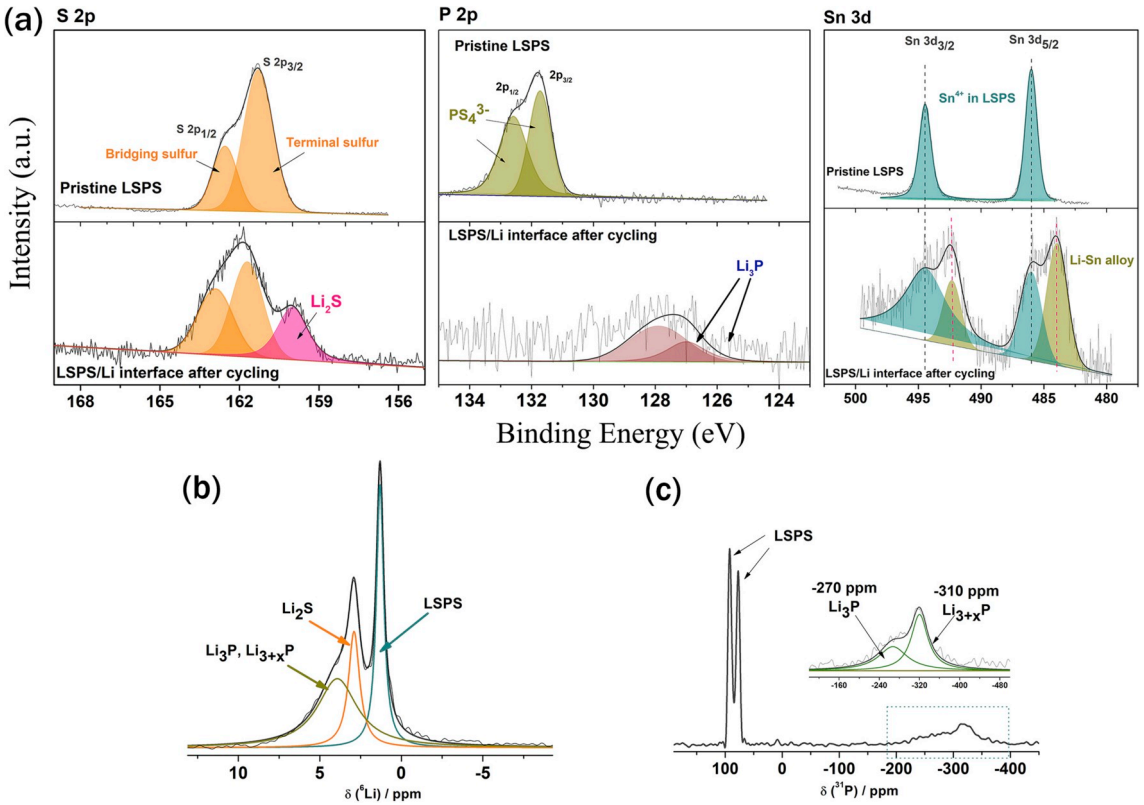

Fig. 8. (a) X-ray photoelectron spectra of the pristine LSPS and the cycled Li metal. (b) ^{6}Li, (c) ^{31}P MAS NMR spectra of the cycled LSPS.

generation of Li_4SnS_4 and Li_3PS_4 with lower ionic conductivity. Therefore, it is critical to consider the possible side-effects of cathode processing methods on the preparation of all solid-state batteries, especially for the unstable sulfide solid electrolyte system. In addition, the low initial coulombic efficiency and unacceptable capacity fading with cycles in LSPS based all-solid-state battery also hinder the practical applications of LSPS sulfide solid electrolyte. We provide detailed investigation on the interfacial reactions at both cathode and anode sides. Our results indicate that when charged to 4.2 V, LSPS is oxidized into S, SnS_2 and P_2S_5. In addition, a mixed conducting interphase composed of Li-Sn alloy, Li_2S and Li_3P formed at LSPS/Li metal anode interface during cycling is detrimental to the long-term cycle performance of batteries. Furthermore, the rough and porous morphology of the cycled LSPS is demonstrated as the main factor accounting for the increase of the LSPS/Li interfacial resistance. Our work highlights that LSPS sulfide solid electrolyte is still facing several challenges in all-solid-state batteries, including not only chemical and electrochemical instabilities, but also how to establish a good interfacial contact and maintain this compact contact during the volumetric expansion of the interface upon battery cycling. It is imperative to design solid electrolytes with stable interfacial layers with relevant electrode materials or to introduce an artificial layer between SSEs and electrodes allowing stable and intimated interfacial contact.

Declaration of competing interest

The authors declare no conflict of interest.

Acknowledgements

This work is financially supported by National Key Research and Development Program of China (grant no. 2018YFB0905400) and National Natural Science Foundation of China (grant no. 21761132030, no. 21621091 and no. 21935009).

Appendix A. Supplementary data

Supplementary data to this article can be found online at https://doi.org/10.1016/j.nanoen.2019.104252.

References

[1] A. Manthiram, X. Yu, S. Wang, Lithium battery chemistries enabled by solid-state electrolytes, Nat. Rev. 2 (2017) 16103.
[2] Y. Kato, S. Hori, T. Saito, K. Suzuki, M. Hirayama, A. Mitsui, M. Yonemura, H. Iba, R. Kanno, High-power all-solid-state batteries using sulfide superionic conductors, Nat. Energy 1 (2016) 16030.
[3] N. Kamaya, K. Homma, Y. Yamakawa, M. Hirayama, R. Kanno, M. Yonemura, T. Kamiyama, Y. Kato, S. Hama, K. Kawamoto, A. Mitsui, A lithium superionic conductor, Nat. Mater. 10 (2011) 682–686.
[4] Y.S. Jung, D.Y. Oh, Y.J. Nam, K.H. Park, Issues and challenges for bulk-type All-solid-state rechargeable lithium batteries using sulfide solid electrolytes, Isr. J. Chem. 55 (2015) 472–485.
[5] Y. Zhu, X. He, Y. Mo, First principles study on electrochemical and chemical stability of solid electrolyte-electrode interfaces in all-solid-state Li-ion batteries, J. Mater. Chem. 4 (2016) 3253–3266.
[6] W.D. Richards, L.J. Miara, Y. Wang, J.C. Kim, G. Ceder, Interface stability in solid-state batteries, Chem. Mater. 28 (2016) 266–273.
[7] F. Han, T. Gao, Y. Zhu, K.J. Gaskell, C. Wang, A battery made from a single material, Adv. Mater. 27 (2015) 3473–3483.
[8] G. Oh, M. Hirayama, O. Kwon, K. Suzuki, R. Kanno, Bulk-type All solid-state batteries with 5 V class $LiNi_{0.5}Mn_{1.5}O_4$ cathode and $Li_{10}GeP_2S_{12}$Solid electrolyte, Chem. Mater. 28 (2016) 2634–2640.
[9] S. Wenzel, S. Randau, T. Leichtweiß, D.A. Weber, J. Sann, W.G. Zeier, J. Janek, Direct observation of the interfacial instability of the fast ionic conductor $Li_{10}GeP_2S_{12}$ at the lithium metal anode, Chem. Mater. 28 (2016) 2400–2407.
[10] P. Bron, S. Johansson, K. Zick, J. Schmedt auf der Gunne, S. Dehnen, B. Roling, $Li_{10}SnP_2S_{12}$: an affordable lithium superionic conductor, J. Am. Chem. Soc. 135 (2013) 15694–15697.
[11] S.P. Ong, Y. Mo, W.D. Richards, L. Miara, H.S. Lee, G. Ceder, Phase stability, electrochemical stability and ionic conductivity of the $Li_{10\pm1}MP_2X_{12}$(M = Ge, Si, Sn, Al or P, and X = O, S or Se) family of superionic conductors, Energy Environ. Sci. 6 (2013) 148–156.
[12] K. Suzuki, D. Kato, K. Hara, T.-a. Yano, M. Hirayama, M. Hara, R. Kanno, Composite sulfur electrode prepared by high-temperature mechanical milling for use in an all-solid-state lithium–sulfur battery with a $Li_{3.25}Ge_{0.25}P_{0.75}S_4$ electrolyte, Electrochim. Acta 258 (2017) 110–115.

[13] X. Yao, N. Huang, F. Han, Q. Zhang, H. Wan, J.P. Mwizerwa, C. Wang, X. Xu, High-performance all-solid-state lithium–sulfur batteries enabled by amorphous sulfur-coated reduced graphene oxide cathodes, Adv. Energy Mater. 7 (2017), 1602923.
[14] K. Suzuki, D. Kato, K. Hara, T.-a. Yano, M. Hirayama, M. Hara, R. Kanno, Composite sulfur electrode for all-solid-state lithium–sulfur battery with Li_2S-GeS_2-P_2S_5-based thio-LISICON solid electrolyte, Electrochemistry 86 (2018) 1–5.
[15] K. Suzuki, N. Mashimo, Y. Ikeda, T. Yokoi, M. Hirayama, R. Kanno, High cycle capability of all-solid-state lithium–sulfur batteries using composite electrodes by liquid-phase and mechanical mixing, ACS Appl. Energy Mater. 1 (2018) 2373–2377.
[16] M. Kaus, H. Stöffler, M. Yavuz, T. Zinkevich, M. Knapp, H. Ehrenberg, S. Indris, Local structures and Li ion dynamics in a $Li_{10}SnP_2S_{12}$-based composite observed by multinuclear solid-state NMR spectroscopy, J. Phys. Chem. C 121 (2017) 23370–23376.
[17] H. Eckert, Z. Zhang, J.H. Kennedy, Structural transformation of non-oxide chalcogenide glasses. The short-range order of Li_2S-P_2S_5 glasses studied by quantitative ^{31}P and $^{6,7}Li$ high-resolution solid-state NMR, Chem. Mater. 2 (1990) 273–279.
[18] C. Dietrich, D.A. Weber, S.J. Sedlmaier, S. Indris, S.P. Culver, D. Walter, J. Janek, W.G. Zeier, Lithium ion conductivity in Li_2S–P_2S_5 glasses – building units and local structure evolution during the crystallization of superionic conductors Li_3PS_4, $Li_7P_3S_{11}$ and $Li_4P_2S_7$, J. Mater. Chem. 5 (2017) 18111–18119.
[19] T. Kaib, S. Haddadpou, M. Kapitein, P. Bron, C. Schröder, H. Eckert, B. Roling, S. Dehnen, New lithium chalcogenidotetrelates, LiChT: synthesis and characterization of the Li^+-Conducting tetralithium ortho-sulfidostannate Li_4SnS_4, Chem. Mater. 24 (2012) 2211–2219.
[20] A. Hayashi, S. Hama, H. Morimoto, M. Tatsumisago, T. Minami, Preparation of Li_2S–amorphous solid electrolytes by mechanical milling, J. Am. Ceram. Soc. 84 (2001) 477–479.
[21] R. Koerver, I. Aygün, T. Leichtweiß, C. Dietrich, W. Zhang, J.O. Binder, P. Hartmann, W.G. Zeier, J. Janek, Capacity fade in solid-state batteries: interphase formation and chemomechanical processes in nickel-rich layered oxide cathodes and lithium thiophosphate solid electrolytes, Chem. Mater. 29 (2017) 5574–5582.
[22] Z.X. Huang, Y. Wang, B. Liu, D. Kong, J. Zhang, T. Chen, H.Y. Yang, Unlocking the potential of SnS_2: transition metal catalyzed utilization of reversible conversion and alloying reactions, Sci. Rep. 7 (2017) 41015.
[23] C. Peng, H. Chen, G. Zhong, W. Tang, Y. Xiang, X. Liu, J. Yang, C. Lu, Y. Yang, Capacity fading induced by phase conversion hysteresis within alloying phosphorus anode, Nano Energy 58 (2019) 560–567.
[24] G. Nazri, Preparation, structure and ionic conductivity of lithium phosphide, Solid State Ion. (1989) 97–102.
[25] Z. Lin, Z. Liu, N.J. Dudney, C. Liang, Lithium superionic sulfide cathode for all-solid lithium-sulfur batteries, ACS Nano 7 (2013) 2829–2833.
[26] A. Dunst, V. Epp, I. Hanzu, S.A. Freunberger, M. Wilkening, Short-range Li diffusion vs. long-range ionic conduction in nanocrystalline lithium peroxide Li_2O_2—the discharge product in lithium-air batteries, Energy Environ. Sci. 7 (2014) 2739–2752.
[27] Y. Zhang, Q. Cui, X. Zhang, W.C. McKee, Y. Xu, S. Ling, H. Li, G. Zhong, Y. Yang, Z. Peng, Amorphous Li_2O_2: chemical synthesis and electrochemical properties, Angew. Chem. Int. Ed. 55 (2016) 10717–10721.
[28] B. Zheng, J. Zhu, H. Wang, M. Feng, E. Umeshbabu, Y. Li, Q.-H. Wu, Y. Yang, Stabilizing $Li_{10}SnP_2S_{12}$/Li interface via an in situ formed solid electrolyte interphase layer, ACS Appl. Mater. Interfaces 10 (2018) 25473–25482.

Bizhu Zheng is currently a Ph. D. candidate in Collaborative Innovation Center of Chemistry for Energy Materials, College of Chemistry and Chemical Engineering, Xiamen University under the supervision of Prof. Yong Yang. She received her Bachelor's degree in Chemistry from Xiamen University in 2015. Her research interests focus on the interfacial modification in all-solid-state lithium batteries.

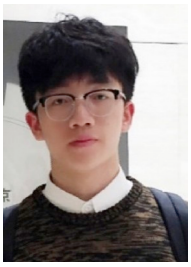

Xiangsi Liu received his Bachelor's degree in Nanjing University of Aeronautics and Astronautics in 2017. He is now pursuing his Ph.D. in School of Chemistry and Chemical Engineering, Xiamen University supervised by Pro. Yong Yang. His research focuses on understanding the reaction mechanism of LIBs and NIBs by solid-state NMR, and developing high-performance energy storage materials.

Jianping Zhu received his B.S in chemistry from Xiamen University in 2016. He is currently a Ph.D. candidate in Collaborative Innovation Center of Chemistry for Energy Materials in Xiamen University since 2016, under the supervision of Prof. Yong Yang. His research focus on energy storage materials and solid lithium batteries.

Jun Zhao is currently pursuing his Ph.D. degree in Clean Nano Energy Center, State Key Laboratory of Metastable Materials Science and Technology, Yanshan University, Qinhuangdao, China. He received his Bachelor's degree and Master's degree in Materials science and Engineering in Wuhan University of Technology in 2016 and 2018, respectively. His research focuses on the in situ TEM/FIB observation of electrochemical behaviors of nanomaterials.

Guiming Zhong obtained his Ph. D. degree in Physical Chemistry from Xiamen University in China in 2013. Currently he is Associate Research Scientist at Xiamen Institute of Rare Earth Materials and Fujian Provincial Key Laboratory of Nanomaterials, Chinese Academy of Sciences. His research focuses on the fundamental understanding of reaction mechanism, local structure and ionic dynamics of energy storage materials through in situ spectroscopic techniques including solid-state NMR, XRD, XAFS, etc. and developing high energy and power density energy storage materials for LIBs and SIBs.

Yuxuan Xiang received his Bachelor's degree in Nanjing University of Aeronautics and Astronautics in 2016. He is now pursuing his Ph.D. in School of Chemistry and Chemical Engineering, Xiamen University supervised by Pro. Yong Yang. His research focuses on the study and application of solid-state NMR and MRI methods in the energy storage system (such as Li and Na ion batteries) and materials.

Hongchun Wang is currently a Ph.D. candidate in Prof. Yong Yang's group at the Xiamen University. He received his Bachelor's degree in Thermal Energy and Dynamical Engineering from University of Science & Technology Beijing in 2014. His current research is focused on developing garnet-like solid Li ion electrolytes for all solid-state Li ion batteries.

Weimin Zhao worked as a R&D engineer (2010–2015) in Tianjin Jinniu power sources Co., Ltd after received his master degree in Applied Chemistry(2010) from Guilin University of Technology, China. He is currently a Ph. D. candidate under the supervision of Prof. Yong Yang in College of Energy, Xiamen University. His research interests primarily focus on novel electrolyte additives development and fundamental understanding of interface mechanisms for high performance LIBs.

Ediga Umeshbabu received his PhD degree from Indian Institute of Technology (IIT) Madras, India in 2016. Later on, he joined Prof. Yong Yang's research group as a postdoctoral research associate at Xiamen University, China. His main research interests are the development of high capacity and high energy density cathode materials for all-solid-state lithium batteries, including lithium-sulfur and lithium-ion batteries.

Qi-Hui Wu obtained PhD degree in 2003 from Darmstadt University of Technology, Germany, then did postdoctorial researches at Georgia Institute of Technology and Ruhr Bochum University, respectively. In 2005, he joined Xiamen University as an Associate Professor, in 2007 he worked at Bonn University as an Alexander von Humboldt (AvH) Fellow, and 2008 at La Trobe University as a Senior Research Fellow, 2011 at City University of Hong Kong as a Research Fellow. Currently, He is a Professor of Materials Science at Jimei University. His research topics include surface science & engineering, and energy materials. He has published about 130 journal articles.

Jianyu Huang is currently a Professor at Yanshan University, Qinhuangdao, China. He received his BS from Xiangtan University in 1990 and PhD from Institute of Metal Research, Chinese Academy of Sciences in 1996. He primarily concentrates on the research of in situ electron microscopy of nanostructured materials. He intends to bridge the gap between microstructure characterizations and property measurements by conducting integrated studies on the microstructure and electrical, mechanical, thermal, optical and electrochemical properties of individual nanostructures, such as carbon nanotubes, nanowires and nanoparticles.

Yong Yang is a distinguished professor in Chemistry in the State Key Lab for Physical Chemistry of Solid Surface at Xiamen University. He also serves as Editor for J Power Sources and Board Member of International Battery Materials Association (IBA) and International Meeting of Lithium Battery (IMLB). His main research interests are new electrode/electrolyte materials for Li/Na-ion batteries, *in-situ* spectroscopic techniques, and interfacial reaction mechanism study in electrochemical energy storage and conversion system.